Float Observations of the Southern Ocean. Part I: Estimating Mean Fields, Bottom Velocities, and Topographic Steering

SARAH T. GILLE

Scripps Institution of Oceanography, and Department of Mechanical and Aerospace Engineering, University of California, San Diego, La Jolla, California

(Manuscript received 21 September 2001, in final form 13 September 2002)

ABSTRACT

Autonomous Lagrangian Circulation Explorer (ALACE) floats are used to examine mean flow and eddy fluxes at 900-m depth in the Southern Ocean. Mean temperature and dynamic topography from float data are consistent with earlier estimates from hydrographic surveys, although floats imply warmer temperatures and narrower frontal structures than do atlas data. Differences between hydrographic and ALACE dynamic topography suggest the presence of eastward bottom velocities of about 2 cm s^{-1} below the eastward-flowing jets of the Antarctic Circumpolar Current. Flow is steered by bathymetry and can be represented as an equivalent barotropic system with an *e*-folding depth of about 700 m.

1. Introduction

The Antarctic Circumpolar Current (ACC) is the oceanic pathway carrying water and tracers between the Pacific, Atlantic, and Indian Oceans. The relevance of the ACC for global heat budgets (and ultimately for climate) depends both on the absolute strength of the current and on the fluxes that mix water from the subtropics into and across the ACC. Autonomous Lagrangian Circulation Explorer (ALACE) floats provide data to address both of these questions. This paper considers the mean temperature and flow fields seen by floats, while a companion paper (Gille 2003) looks at the eddy heat and momentum fluxes that can be inferred from floats.

Past estimates from hydrography and current meters have indicated that in Drake Passage the ACC has a mean transport of $134 \pm 13 \times 10^6$ m^3 s^{-1} concentrated in two or three narrow jets (Nowlin and Klinck 1986). Direct current meter measurements imply that the velocity in the jets is eastward at all depths, with no reversal anywhere in the water column (e.g., Whitworth et al. 1982), and so transport estimates from hydrographic data have typically been referenced to the bottom or to the deepest common level (e.g., Georgi and Toole 1982; Whitworth and Nowlin 1987). Recent analysis of direct velocity measurements from acoustic Doppler current profilers (ADCPs) and current meters have suggested that within the core of the ACC jets, barotropic (or bottom) velocities may be 4–10 cm s^{-1} eastward, resulting in larger transports at the core of the jets (B. King 1998, personal communication; Donohue et al. 2000; Phillips and Rintoul 2002). However, ADCP measurements are instantaneous velocity estimates that are strongly influenced by internal waves and tides, and the associated error bars can be as large as the implied transport increases. Current meter measurements also have limitations; although they provide extensive temporal coverage, they are available at only a few isolated locations. In contrast, ALACE floats sample globally, obtaining mean temperatures and velocities over 9–25-day intervals and therefore are averaging over several full tidal and internal wave cycles. One of the design objectives in deploying ALACE floats was to measure absolute reference velocities for use in refining hydrographic transport estimates. The first goal of this study is to make use of ALACE measurements to map mean temperature and dynamic topography in the Southern Ocean. ALACE temperatures are then compared with hydrographic temperatures, and ALACE velocities are used, together with hydrography, to estimate bottom velocities and total time-averaged transport of the ACC.

The second goal of this paper is to examine how topography influences flow in the Southern Ocean. The ACC is known to be steered by bathymetry through fracture zones in the ridges around Antarctica (Kamenkovich 1962; Gordon et al. 1978; Gille 1994), and flow is predicted to follow bathymetric contours (Schulman 1975). ALACE data provide an extensive record of middepth velocities that are used here to evaluate the relative importance of bathymetric steering.

This paper is organized as follows: section 2 discusses

Corresponding author address: Dr. Sarah T. Gille, Scripps Institution of Oceanography, University of California, San Diego, La Jolla, CA 92093-0230.
E-mail: sgille@smtp.ucsd.edu

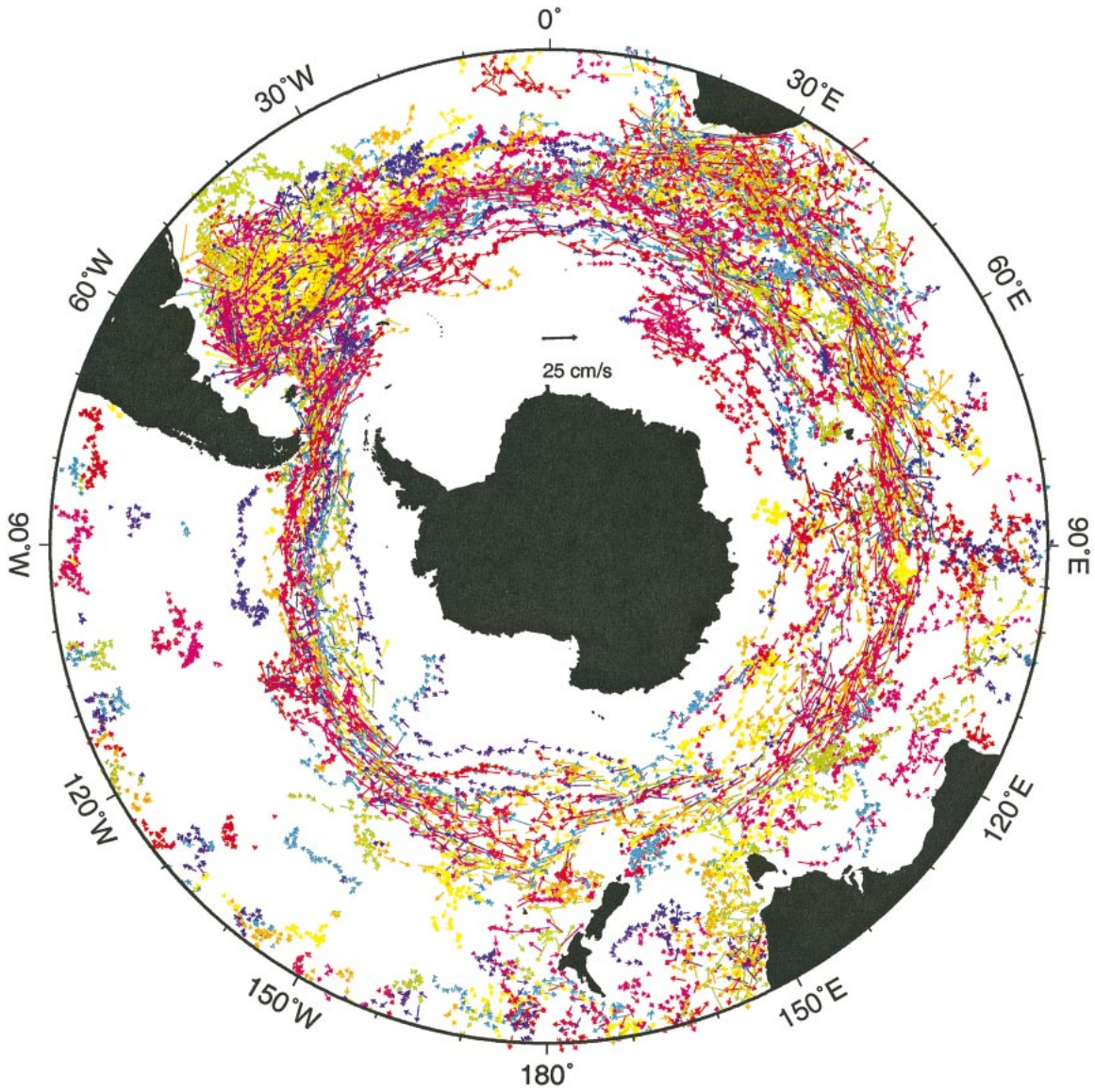

FIG. 1. Velocities derived from 12 941 ALACE float displacements in the Southern Ocean. Roughly two-thirds of these measurements include PALACE float profiles. Repeated displacements of the same float are the same color. Vectors indicate mean velocities as indicated by the scale, and vector lengths do not vary as a function of latitude. Most of these Southern Ocean floats show strong zonal velocities, indicating that they have been carried by the ACC.

the ALACE floats used in this study and the hydrographic atlas data that are compared with the floats. Mean objectively mapped temperature fields are discussed in section 3. Transport estimates and bottom velocities are discussed in section 4, with supplemental discussion of the objective mapping technique in the appendix. Section 5 examines the mean flow response to bathymetry. The results are summarized in section 6.

2. ALACE floats and atlas data

ALACE floats were deployed in the Southern Ocean as part of the World Ocean Circulation Experiment (WOCE) starting in 1990 (Davis et al. 1996). As Lagrangian devices, they sample both in space and time. Figure 1 shows the subsurface displacements of all ALACE and Profiling ALACE (PALACE) floats available in the Southern Ocean. ALACE floats are designed to follow the current at a fixed pressure (in this case about 900 dbar), although they do not actively control their depths. At fixed time intervals (here 9–25 days), they rise to the ocean surface and spend a day communicating their position and mean temperature via an Argos transmitter before returning to depth. ALACE floats provide middepth velocities, averaged over a time period comparable to the eddy decorrelation scale (Da-

vis 1998). Since the floats are blown around by the wind while they are at the surface, their long-term trajectories may not be physically meaningful, and each vector is therefore treated as an independent velocity estimate. PALACE floats closely resemble ALACE floats but have the additional capability to profile temperature and in some cases salinity as they ascend or descend (Davis et al. 2001). Profiles are not analyzed in this paper.

A total of 12 941 float velocities from the Southern Ocean were used for this investigation. Each of these was between 700 and 1100 dbar deep, with a mean pressure of 889 dbar, median pressure of 895 dbar, and a standard deviation of 86 dbar. Of these, 12 616 had usable temperature information, with a mean of 3.9°C, a median of 3.4°C, and a standard deviation of 1.7°C. Most of the floats cycled at intervals of 9, 10, or 25 days; 51% had cycle times of 20 days or longer, and 44% had cycle times between 8 and 11 days. Velocity information from ALACE was compared with geostrophic velocities from hydrographic data; comparisons between geostrophic velocities and float velocities were carried out only for the 10 805 subsurface displacements from regions that were at least 3000 m deep, so that velocities could be referenced consistently to a common depth.

Although the floats span 400 m in depth, this analysis depends on having temperature and velocity from a single common depth. For this study, ALACE-measured pressures were converted to depths (Saunders and Fofonoff 1976). Since different float groups were engineered to sink to different depths, and floats did not necessarily end up at their design depth, the local vertical gradient of potential temperature in atlas data (Gouretski and Jancke 1998, henceforth GJ) was used to apply a linear correction to the potential temperature in order to provide temperature at 900-m depth. The variance of potential temperature decreases with depth, and so this procedure results in a net increase in the variance of potential temperature. Similarly, the vertical gradient of geostrophic velocity was used to rescale measured ALACE velocities in order to represent flow at 900-m depth. These corrections are considerably simpler than standard mooring motion corrections, which allow temperature and velocity to have a canonical polynomial profile (e.g., Hogg 1991). For the global Southern Ocean, available data are inadequate to determine an appropriate, geographically varying temperature profile, and existing hydrographic profiles suggest that at 900 m temperature and geostrophic velocity both decrease nearly linearly with depth.

Comparison hydrographic data for this study comes from GJ's atlas. This atlas uses data held by the National Ocean Data Center (NODC), but it differs from the National Oceanic and Atmospheric Administration (NOAA) atlases (Levitus and Boyer 1994; Levitus et al. 1998; Antonov et al. 1998) in a number of ways. Gouretski and Jancke supplemented the NODC data with recent measurements from WOCE and other field programs, including some data that were still considered proprietary. Temperature and salinity data were mapped on neutral density surfaces to avoid producing artificial water masses, and high vertical resolution was used to reduce data loss near the bottom. Last, GJ produced gridded fields using the objective mapping algorithm described by Bretherton et al. (1976). This provides a best estimate of the time-mean temperature and salinity from irregularly spaced data and includes a formal error estimate for the gridded data. To produce their atlas, GJ first averaged the data in 30 km × 30 km boxes. Averaged data were objectively mapped using a Gaussian decorrelation function with an *e*-folding scale of 500 km and assuming a signal-to-noise ratio of 1. Results were output on a 1° × 1° grid.

For this study, dynamic topography at 900 m was computed from GJ's gridded temperature and salinity fields and referenced to depths between 3000 and 4000 m. Because many of the Southern Ocean ridges are between 3000 and 4000 m deep, dynamic topography can be computed at many more locations relative to 3000 m than relative to deeper reference levels. At locations where dynamic topography could be referenced to 3000 m (D_{3000}) but not to a deeper level (D_{3500} or D_{4000}), an artificial dynamic topography field was created by filling gaps statistically: For each missing point, all data within ±10° of the gap were used in a linear regression of D_{3000} versus D_{3500} or D_{4000}. The resulting regression coefficients are a constant, c, and a linear slope, λ, and the missing dynamic height value is $\hat{D}_{3500} = c + \lambda D_{3000}$.

The error bars of any objective map depend on a priori assumptions about the measurement variance and the signal-to-noise ratio of the data. Gouretski and Jancke produced percent errors but did not assign absolute errors to their values. In order to use ALACE data in combination with the GJ atlas, consistent error bars were needed for both types of data. For this analysis, the measurement variance was assumed to be determined largely by time variability at each location because instrumental errors are small as compared with measured variability. Modern calibrated CTD temperature measurements have an uncertainty of 0.002°C. Similarly, thermistors used by ALACE are calibrated with an accuracy of 0.001°–0.003°C, and the sensor drift is expected to be less than 0.001°C yr^{-1} (R. E. Davis 2001, personal communication). Numerical truncation required to transmit temperatures via satellite can in some cases slightly reduce the precision of the measurements.

In contrast to the small instrumental errors, temperature variance within a small geographic location is significant. NODC temperature records at 900-m depth have a standard deviation of 0.3°C within 1° latitude by 2.5° longitude boxes that contain at least four samples. Therefore, for both atlas and ALACE measurements, the ''noise'' due to temporal variability is assumed to be 0.3°C. The temperature signal is assumed to be related to the large-scale temperature gradient, which has a root-mean-squared (rms) meridional gradient of 0.3

degrees Celsius per degree of latitude in atlas data between 40° and 60°S. This change per degree is comparable to the noise, but local frontal features are steeper than the smoothed atlas data indicate, implying a signal-to-noise ratio greater than 1. For this study, signal-to-noise ratios between 1 and 4 were tested, and a signal-to-noise ratio of 2 was used as the basic case.

Formal statistical errors for a mean quantity scale with $1/\sqrt{N}$, where N is the number of samples. Floats provide multiday, continuous averages of temperature and velocity, so the duration of each displacement, δt might be thought of as a proxy for N, suggesting that formal error bars should be proportional to $1/\sqrt{\delta t}$. In this case, since the exact structure of the temporal variability was not well defined, no adjustment was made to error bars to account for the duration of the ALACE displacements.

Dynamic topography noise, like temperature noise, can be attributed to time-dependent variations in the observed fields rather than instrumental errors. Uncertainties in atlas dynamic topography depend on the spatial distribution of hydrographic station data used to map temperature and salinity. One might imagine that dynamic height should have a smaller percentage error than does temperature because dynamic height represents a summation of observations from a range of different depths. However, in reality, temperature and salinity data distributions are nearly the same at all depths and, as a result, gridded temperature and salinity are likely to be biased consistently throughout the water column relative to ''true'' data values. Therefore, for this study, GJ's percent errors for temperature were used to represent atlas dynamic topography percent errors. The following procedure was followed to assign uncertainties: first, TOPEX altimeter rms sea surface height variability was determined to be 0.085 m in the Southern Ocean. Dynamic topography at 900-m depth has one-half as much range as dynamic topography at the surface, and so the rms dynamic topography at 900-m depth was inferred to be 0.04 m. For comparison, in the Southern Ocean, dynamic topography at 900-m depth has an rms meridional gradient of 0.04 meters per degree of latitude in smoothed atlas data. Larger meridional gradients are expected near major frontal features. Dynamic height signal-to-noise ratios are therefore assumed to lie in the same range as temperature signal-to-noise ratios.

ALACE dynamic topography is derived from velocity data. Positions at the start and end of the ALACE displacement are determined to ± 3 km (Davis 1998), implying a velocity uncertainty of 0.002 m s^{-1} over 25 days [and a corresponding error in sea surface height gradient of about 0.002 m $(100\ km)^{-1}$]. These instrumental errors are considerably smaller than the variance implied by altimetry, and so the hydrographic rms noise value of 0.04 m was also assigned to ALACE dynamic height covariance estimates.

3. Mean temperature: Evidence for Southern Ocean warming

ALACE floats, with their combined measurements of middepth temperature and velocity, offer a direct window on subsurface ocean circulation. By following the flow over 9–25-day periods, they are expected to be good estimators of time-averaged temperature and geostrophic reference velocities. This section takes advantage of the decade of temperature measurements from ALACE, as well as a priori assumptions about the error covariance matrix, to estimate mean Southern Ocean temperatures for the 1990s.

a. Case A: The basic temperature map

Temperatures from ALACE were objectively mapped using the Bretherton et al. (1976) technique. The same method was employed for the GJ fields and has been used in previous studies of ALACE measurements (e.g., Davis 1998). In this study, each ALACE measurement was treated as an independent observation, and separate displacements were not averaged prior to mapping. Following the methodology outlined by Bretherton et al. (1976), mean temperatures estimated directly from the data were subtracted prior to objective mapping and added back into the data fields to obtain the final temperature maps. Figure 2a shows mean temperature at 900 m from GJ, and Fig. 2b shows mean float temperature obtained by objectively mapping the ALACE observations that have been projected to 900-m depth. Both fields were computed using the same isotropic Gaussian covariance function, with an *e*-folding scale of 500 km. This basic case is identified as case A, and the parameters used for this mapping are summarized in Table 1. Although atlas data were mapped using a signal-to-noise ratio of 1, for ALACE data, a signal-to-noise ratio of 2 was selected for the basic case. Ratios of 1 and 4 were also tested (see cases G and H).

The resulting temperature fields from atlas and ALACE are qualitatively similar, with an average temperature range of 3.3°C between 40° and 60°S. Figure 3a shows the difference between the hydrographic and float temperature fields. The maximum temperature difference between the two fields is 3.1°C and is associated with the Agulhas Retroflection, which does not appear in the mapped hydrographic data. In regions with formal mapping errors of less than 0.15°C, float temperatures are on average 0.15°C warmer than atlas temperatures, and the rms difference between the fields is 0.38°C. The mean temperature difference is greater south of 45°S, in part because ALACE floats are not designed to sample under the ice and do not capture the southernmost temperatures of the Southern Ocean.

The major cause of the differences between mapped hydrographic data and ALACE observations is a long-term warming trend, which has increased average mid-

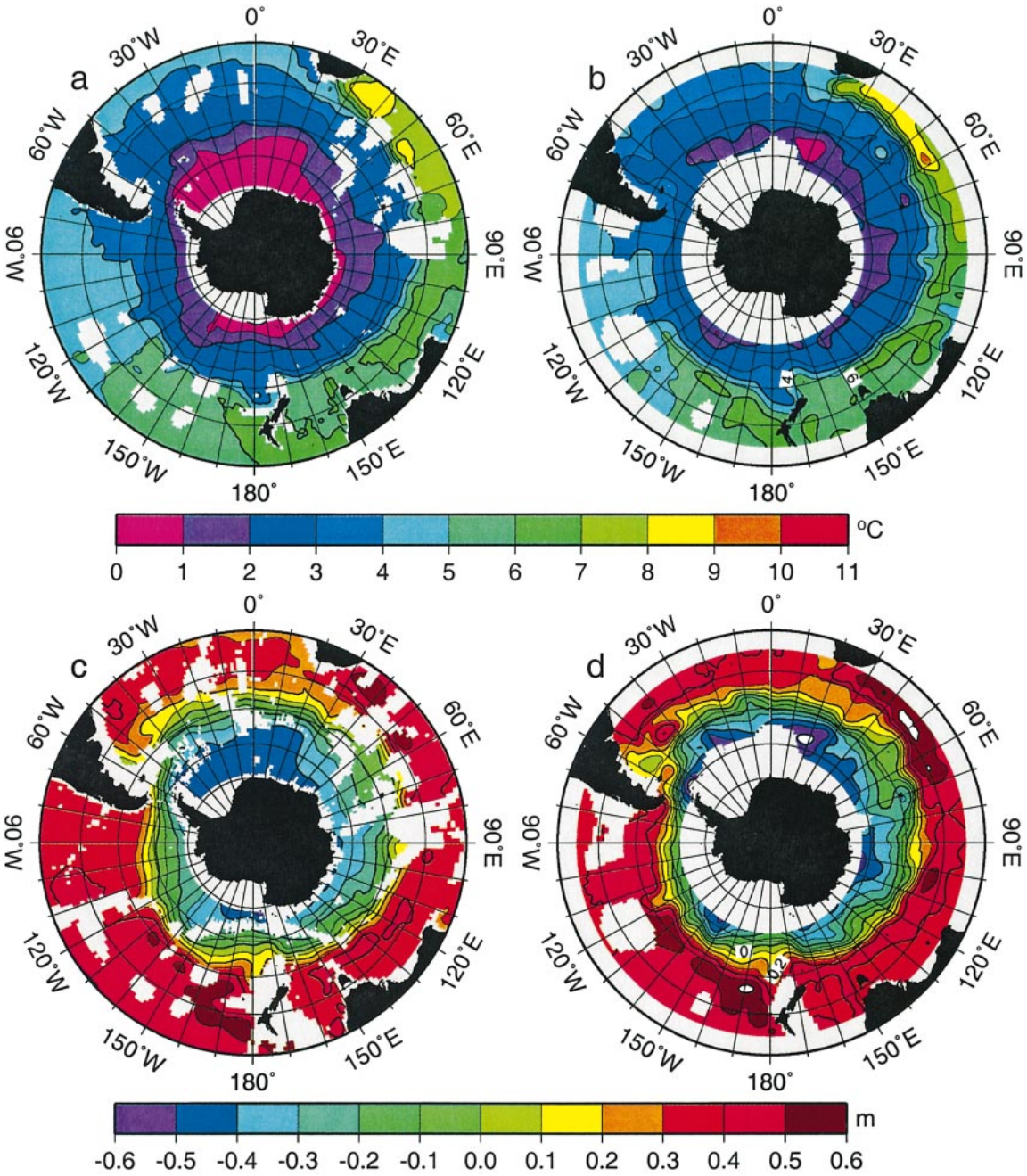

FIG. 2. Objectively mapped (a), (b) temperature and (c), (d) dynamic topography at 900-m depth from (a), (c) hydrographic atlas data and (b), (d) ALACE. Dynamic topography from (c) hydrographic data is referenced to 3500-m depth. Here both atlas and ALACE fields were initially objectively mapped using an isotropic Gaussian decorrelation function, with an *e*-folding scale of 500 km as specified in case A of Table 1. Signal-to-noise ratios were set to 1 in atlas maps and to 2 in ALACE maps. Regions with formal errors of greater than 50% of the standard deviation are not mapped. Thus the maximum formal uncertainties of the mapped fields are 0.15°C for temperature maps and 0.02 m for dynamic height maps.

depth temperatures in the Southern Ocean by approximately 0.2°C since the 1950s (Gille 2002). Float data indicate warmer temperatures particularly within the southern portion of the Southern Ocean, suggesting that the temperature gradient associated with the ACC may be farther south in the float data than it is in the hydrography. Some of the warming trend may also be associated with a temperature increase on individual water parcels (Gille 2002). Overall, the trend is consistent with warming seen in the Pacific sector of the Southern Ocean in WOCE data relative to previous observations (Swift 1995).

TABLE 1. Mapping parameters used and resulting differences between hydrographic (atlas) T_a and float T_f temperature maps. Errors in mean are standard errors and are equal to the standard deviation (std) of the temperature difference divided by $\sqrt{N}$ and multiplied by 5 to account for the roughly 5° decorrelation length scale in both x and y directions. Results shown are for locations with formal errors estimated to be less than 0.5 times the a priori standard deviation (i.e., less than 0.15°C). Case M represents the merger of objectively mapped fields derived separately from hydrographic and float data. Temperature differences between case-M fields and hydrographic maps are included for completeness but are necessarily smaller than differences between float temperatures and hydrographic maps.

Case	L_x (km)	L_y (km)	L_T (dynamic m)	S/N	D_{ref} (m)	$\langle T_a - T_f \rangle$ (°C)	std($T_a - T_f$) (°C)
A	495	495	∞	2	3500	−0.16 ± 0.02	0.38
B	1100	1100	∞	2	3500	−0.19 ± 0.02	0.39
C	880	440	∞	2	3500	−0.15 ± 0.02	0.37
D	440	220	∞	2	3500	−0.16 ± 0.02	0.40
E	220	440	∞	2	3500	−0.16 ± 0.02	0.41
F	220	110	∞	2	3500	−0.20 ± 0.02	0.45
G	495	495	∞	1	3500	−0.16 ± 0.02	0.37
H	495	495	∞	4	3500	−0.15 ± 0.02	0.38
I	495	495	0.4	2	3500	−0.15 ± 0.02	0.38
J	495	495	∞	2	3000	Same as A	
K	495	495	∞	2	4000	Same as A	
M	495	495	∞	2	3500	−0.03 ± 0.01	0.15

b. Variations: Sensitivity to mapping parameters

Results are sensitive to the specific choice of decorrelation scale and signal-to-noise ratio used for mapping. In order to evaluate the robustness of mapped dynamic topography, additional objective maps were computed from ALACE data. Table 1 summarizes the different mapping parameters tested and the rms temperature difference between atlas and mapped float temperatures. In temperature cases B–F, zonal and meridional decorrelation length scales (L_x and L_y) were varied. Isotropic and anisotropic decorrelation scales ranging from 110 to 1100 km were tested. In cases G and H, the signal-to-noise ratio (S/N) was changed. In addition, as discussed in the appendix, in case I ALACE temperatures were assumed roughly to follow contours of dynamic height from the atlas data. In this case, in addition to the standard 500-km isotropic spatial decorrelation, the covariance also decreased with changes in dynamic height, using an e-folding scale of 0.4 dynamic m.

The eight temperature objective maps corresponding to cases B–I (not shown) closely resemble each other and case A, both in large-scale features and in their mean and rms differences relative to atlas temperatures, as summarized in Table 1. ALACE temperatures are uniformly at least 0.15°C warmer than atlas temperature, indicating that the temperature difference, which is associated with the warming of the ACC, is not strongly sensitive to mapping parameters.

In all cases the rms difference between ALACE and atlas fields is about 0.4°C. In contrast, formal mapping errors for each of the temperature estimates are less than 0.1°C, suggesting that there should be no more than 0.15°C uncertainty in the difference. The rms differences are larger than statistical uncertainties would suggest, partly because of the 0.15°–0.20°C bias between the fields, partly because the temperature differences have non-Gaussian statistics that are dominated by outliers, and partly because statistical uncertainties in the temperature field have been assumed to be geographically uniform for simplicity, although in fact they must vary geographically.

Since ALACE and hydrography provide independent estimates of temperature and error covariance information, best estimate temperatures at 900-m depth can be refined by using a ''recursive update'' scheme (Wunsch 1996) to merge the two fields. The error covariance matrices computed in the separate objective mapping of float and hydrographic data are used to establish optimal temperature and dynamic topography fields and corresponding error covariance matrices. Case M in Table 1 summarizes parameters used for merged fields; since the merged data are a weighted combination of the atlas and ALACE maps, the rms difference between the merged temperatures and atlas temperatures is by definition smaller than the difference between ALACE and atlas temperatures and does not provide information about differences between the fields. Figure 3b shows the results of merging the temperature and dynamic height fields from case A with the corresponding atlas fields to obtain an optimal estimate of time-averaged temperature. Because more data contribute to this map, the formal mapping errors are smaller, and low-error temperatures are estimated for most of the map domain.

4. Mean dynamic height: Evidence for nonzero bottom velocity

a. Dynamic topography

The velocity measurements from ALACE were used to objectively map dynamic topography, following the method of Bretherton et al. (1976). The appendix provides a general formulation of this method and details the adaptations needed for anisotropic and streamfunction-following covariance functions. Figures 2c and 2d compare dynamic height at 900 m relative to 3500 m from GJ with case-A dynamic topography from ALACE. Since the objective mapping algorithm is intended

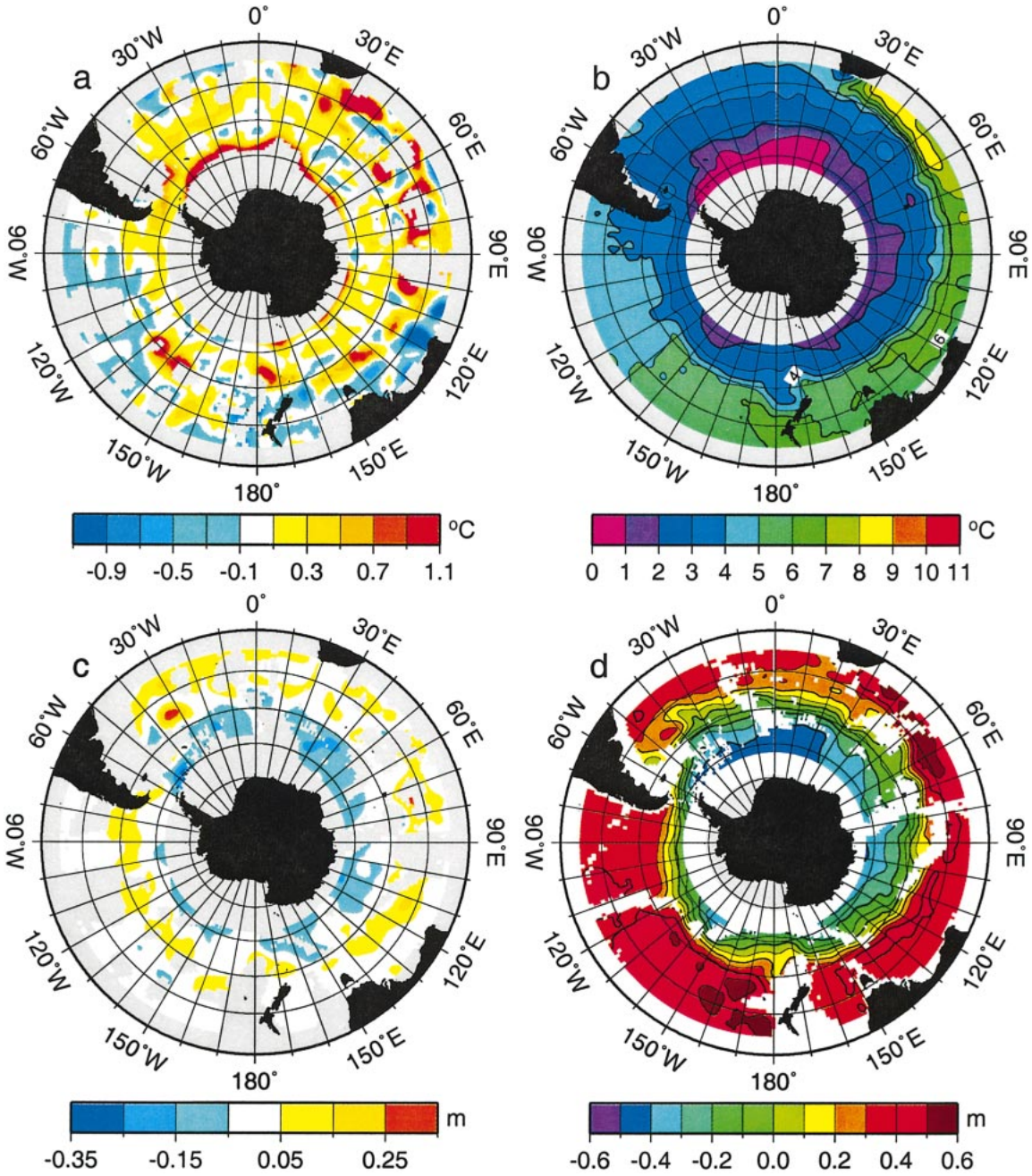

FIG. 3. (a) Float temperature minus atlas temperature, (b) optimal merger of atlas and float temperatures, (c) float dynamic height minus atlas dynamic height, and (d) optimal merger of atlas and float dynamic height. In all cases, fields represent values at 900-m depth, and regions with formal errors greater than 0.5 times the standard deviation are not shown. The text briefly outlines the formal methodology used to merge the fields.

to map anomalies and not nonzero mean fields, an a priori estimate of mean geostrophic velocity was removed from ALACE velocity data prior to objective mapping and an equivalent a priori estimate of dynamic topography was added to the final objectively mapped dynamic topography. The GJ atlas dynamic height $\hat{D}_{3500}$ was used to provide a first guess of geostrophic velocity and mean dynamic topography. The final results will not depend on $\hat{D}_{3500}$ except in locations where ALACE measurements are not available and error bars are large.

In both Figs. 2c and 2d, the large-scale circulation pattern is consistent with large-scale zonal flow with a slight southeastward tendency. The flow undergoes northward excursions near Campbell Plateau (southeast of New Zealand) and on the eastern side of Drake Passage, as described by Gordon et al. (1978). The differ-

ence between the fields is depicted in Fig. 3c, and the optimal merger of the fields, case M, is depicted in Fig. 3d. Because dynamic height is mapped relative to an arbitrary reference position, the mean difference between the two dynamic height fields is zero. In locations where few data are available, such as regions outside the ACC, error bars are large and the objectively mapped field differs negligibly from the reference field derived from atlas data. Local differences between ALACE and atlas maps can be attributed either to differences in the distribution of data available for mapping or to real physical differences as discussed in the next subsection. Sea surface height inferred from ALACE tends to be higher than atlas dynamic topography on the north side of the ACC and lower on the south side. This is consistent with the presence of eastward flow at the 3500-m reference depth used to map the atlas data.

b. Bottom velocities

Dynamic topography from middepth ALACEs represents absolute topography and does not depend on a known reference level. Thus differences between mean geostrophic velocities inferred from ALACE and those derived from atlas data referenced to the bottom can be used to estimate bottom velocities in the Southern Ocean. While preliminary efforts to include ALACE measurements in an inverse model did not significantly influence reference velocity estimates, results suggested that with more data reference velocities might be determined from ALACE (Gille 1999). An order-of-magnitude more ALACE displacements were available for this study than for the earlier inverse model, and corresponding statistical improvements are expected. The GJ atlas data indicate that the top-to-bottom total geostrophic transport through the Southern Ocean averages 150×10^6 m^3 s^{-1} eastward. This quantity is determined by computing net transport between 35° and 62°S at 1° longitude intervals and zonally averaging the results. Bottom velocities inferred from ALACE/atlas differences are highly variable over this latitude range, in part because formal mapping errors can be large where few data are available.

This analysis will focus on the circumpolar flow, defined between dynamic height contours -0.4 and 0.4 m in Fig. 2c. In addition, data are only considered if they come from regions with mapping errors estimated to be less than 50% of the a priori error (shown in color in both Figs. 2c and 2d. This region encompasses the ACC as well as some regions that appear to be outside the ACC.) Since data are mapped on a 1° by 1° grid, zonal bottom velocities are computed for every grid point with low error bars. Mean transports are computed at 1° longitude resolution, and zonal averages are reported here. Because the ACC does not necessarily have an east–west orientation, total velocities may exceed eastward velocities, and transport is likely to be a more robust indicator than velocity of differences between hydrography and floats.

From atlas data, total top-to-bottom circumpolar transport relative to the bottom within this region averages $98 \pm 5 \times 10^6$ m^3 s^{-1}. For all data points with formal mapping error bars of less than 50% of the a priori error, differences between geostrophic velocities computed from atlas data and from case-A ALACE geostrophic velocities imply a mean eastward bottom velocity of 0.3 ± 0.1 cm s^{-1}. For data points that fall between the ± 0.4-m dynamic height contours in Fig. 2c, the mean eastward bottom velocity is 0.4 ± 0.1 cm s^{-1}. To determine the mean eastward transport, these bottom velocities were vertically integrated at each grid point using the local depth. The contribution to the transport from bottom velocities averages $23 \pm 2 \times 10^6$ m^3 s^{-1}. These case-A results are summarized in Table 2. The implied total circumpolar transport is therefore $121 \pm 6 \times 10^6$ m^3 s^{-1}. This is consistent with Drake Passage estimates of $134 \pm 13 \times 10^6$ m^3 s^{-1} that were computed by referencing Drake Passage transports to current meter data (Nowlin and Klinck 1986). However, since high-error-bar regions were discarded from both the hydrographic transport estimates and the bottom velocity estimates, these results may not capture the full width of the circumpolar flow. Elsewhere, the geographic region between the ± 0.4-m dynamic height contours is much wider than the ACC, and so this estimate may encompass recirculations north of the ACC. As a result the ALACE-derived estimates could potentially skew or underestimate the transport.

Most of the effect of these large bottom velocities is confined to the core eastward jets of the ACC. Figure 4 shows the maximum eastward velocity between 35° and 62°S for case A at 1° longitude intervals (dashed line) along with the corresponding bottom velocities directly below the velocity maximum (solid line). Maximum eastward velocities average 8.2 ± 0.1 cm s^{-1}, and the bottom velocity below the jet maximum averages 1.8 ± 0.1 cm s^{-1}. Eastward bottom velocities vary substantially as a function of longitude depending on the depth of the ocean, the orientation of the mean current, and the current speed. Figure 4 indicates that bottom velocities tend to be largest in locations where velocities at 900-m depth are largest.

Figure 2d suggests that the core of the ACC (characterized by closely packed dynamic height contours) is typically about 5° latitude in width. To identify flow in the jet core, at each degree longitude, the five largest eastward velocities at 900-m depth were selected from the 1° gridded data. Although the five velocities were not necessarily contiguous, in general they corresponded to a 5° latitude band representing the peak eastward transport of the ACC core. For case A in Table 2, bottom velocities in the jet core average 1.9 ± 0.2 cm s^{-1}. Zonally averaged eastward geostrophic transport relative to the bottom in this jet core is $59 \pm 3 \times 10^6$ m^3 s^{-1}; the barotropic transport associated with bottom ve-

TABLE 2. Transport (T) and bottom velocity (v_b) dependence on mapping parameters. Cases are as identified in Table 1. Velocity and transport estimates are only considered when error bars are less than 50% of the a priori error. Columns identified as T indicate top-to-bottom geostrophic transport referenced to the bottom from atlas data, and columns labeled ΔT indicate the increase in transport due to nonzero bottom velocities. For each degree of longitude, eastward and westward jets are identified by finding the 5° of latitude with greatest positive and negative velocities at 900 dbar, respectively. Mean v_b represents the mean zonal bottom velocity in all locations where errors are less than 50% of the a priori error. Jet transport represents the transport between the −0.4 and 0.4 dynamic height contours for maps referenced to 3500 m.

	Mean v_b			T	ΔT	T	ΔT	T	ΔT
				Jet (10^6 m^3 s^{-1})		Eastward (10^6 m^3 s^{-1})		Westward (10^6 m^3 s^{-1})	
Case	Jet (cm s^{-1})	Eastward (cm s^{-1})	Westward (cm s^{-1})	±6		±3		±1	
A	0.3 ± 0.1*	1.9 ± 0.2	−1.7 ± 0.3	98	23 ± 2	59	36 ± 2	2	−20 ± 2
B	0.3 ± 0.1	1.2 ± 0.1	−1.0 ± 0.1	99	19 ± 2	61	20 ± 1	0	−12 ± 1
C	0.3 ± 0.1	1.9 ± 0.2	−1.7 ± 0.3	99	24 ± 2	60	35 ± 2	2	−20 ± 2
D	0.2 ± 0.2	2.8 ± 0.4	−2.5 ± 0.3	97	17 ± 2	57	53 ± 3	5	−29 ± 2
E	0.2 ± 0.1	2.0 ± 0.3	−1.8 ± 0.3	98	16 ± 2	59	38 ± 2	2	−21 ± 2
F	0.2 ± 0.3	3.3 ± 0.4	−3.8 ± 0.5	90	8 ± 2	52	61 ± 4	8	−41 ± 3
G	0.3 ± 0.1	1.6 ± 0.2	−1.7 ± 0.3	88	12 ± 1	55	27 ± 2	1	−14 ± 1
H	0.4 ± 0.1	2.2 ± 0.3	−1.7 ± 0.2	100	29 ± 2	59	41 ± 3	2	−22 ± 2
I	1.7 ± 0.2	6.0 ± 0.4	−2.7 ± 0.2	97	109 ± 6	60	113 ± 6	2	−32 ± 2
J	0.2 ± 0.1	1.8 ± 0.2	−1.8 ± 0.3	107	12 ± 2	59	33 ± 2	2	−21 ± 2
K	0.4 ± 0.1	2.0 ± 0.2	−1.6 ± 0.3	60	17 ± 2	59	38 ± 2	2	−19 ± 2
M	−0.2 ± 0.1	0.1 ± 0.1	−0.6 ± 0.2	101	−15 ± 2	57	1 ± 1	0	−9 ± 1

* Errors shown are standard errors of the mean. Formal errors determined from propagating the mapping errors for dynamic height yield bottom velocity uncertainties of about 2 cm s^{-1} at any given location. The impact of the formal error is expected to be small when averaged over all data points.

locities is 36 ± 2 × 10^6 m^3 s^{-1}. The sum of these two implies a total transport of 95 ± 4 × 10^6 m^3 s^{-1}, 60% greater than the transport observed in hydrographic atlas data within the same geographic region.

Correspondingly, outside of the jet core, bottom velocities tend to be small or westward. Flow typifying the region outside the jets was identified at each degree of longitude by locating the five most negative or lowest velocities at 900-m depth. These locations can straddle the ACC core, although most frequently small or westward flow is centered about 5° latitude north of the core eastward flow. In these regions, the average zonal bottom velocity for case A is −1.7 ± 0.3 cm s^{-1}, as shown in Table 2, indicating westward flow at the bottom. Correspondingly in these locations, atlas data indicate that transport relative to the bottom is small and eastward at ~2 × 10^6 m^3 s^{-1}, but barotropic transport due to the bottom flow is westward at −20 ± 2 × 10^6 m^3 s^{-1}.

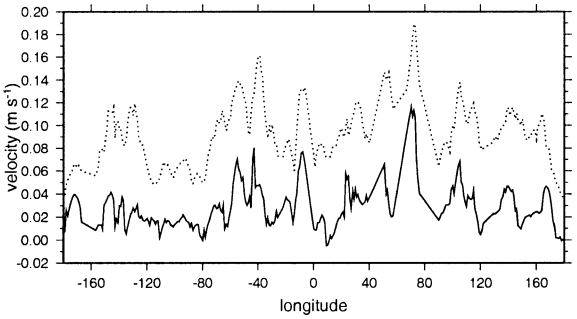

FIG. 4. Maximum eastward zonal velocity at 900-m depth in the ACC latitude band (dashed line) and bottom velocity implied by difference between ALACE and hydrographic dynamic topography (solid line) as a function of longitude. Maximum velocities are selected from data gridded at 1° latitude resolution and represent the single largest zonal velocity at each degree of longitude.

Last, the bottom velocities were examined in the coordinate system of the ACC. Figure 5a shows mean bottom velocities for case A as a function of dynamic height contour. As in Figs. 2c and 2d, the ACC is centered around 0.0 dynamic m. The maximum zonal velocity in Fig. 5a is 1.2 ± 0.3 cm s^{-1}. This is smaller than the mean zonal velocity that occurs below the jet maximum, because the jet is not always fastest at exactly the same dynamic height contour. To the north of the ACC, bottom velocities are negative, indicating consistent westward flow. Figure 5b shows transport as a function of dynamic height. Geostrophic transport relative to the bottom (dashed line) is uniformly positive, while transport that includes the bottom velocity estimates is larger in the core of the ACC but westward to the north of the current core.

As with temperature, objectively mapped dynamic topography is sensitive to the choice of mapping criteria. To evaluate the robustness of the dynamic height maps, the mapping procedure was repeated for each of the parameter combinations used in the temperature maps, as listed in Table 1. In addition, in cases J and K, the reference levels for the initial-guess dynamic height fields were adjusted both to 3000 and to 4000 m. While specific quantitative values depend on the parameters used to define the map, the basic results are robust. Bottom velocities at the core of the ACC are typically

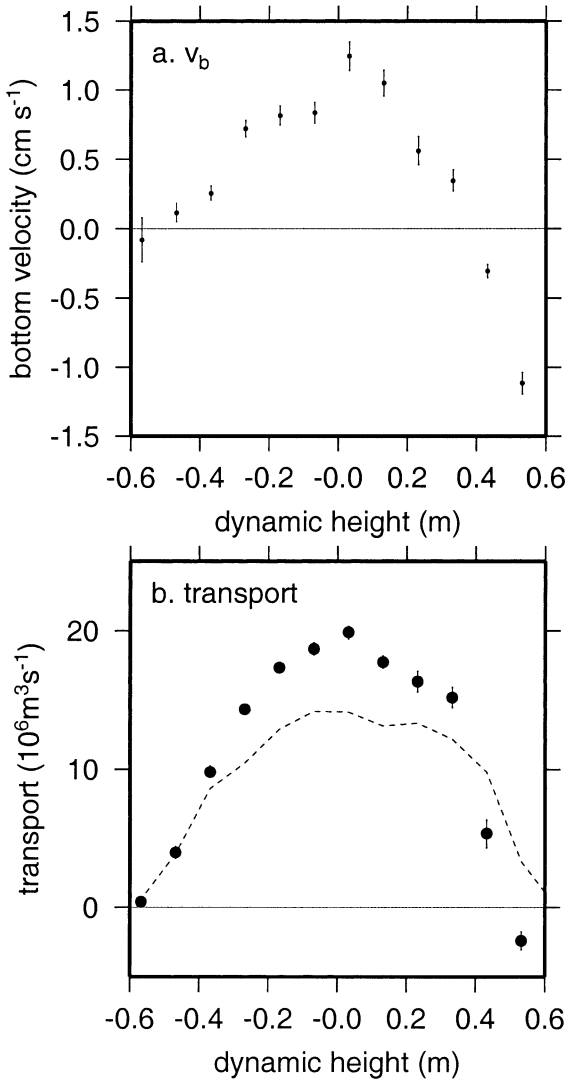

FIG. 5. (a) Mean bottom velocity as a function of dynamic height contour. Error bars represent 1-standard-deviation errors in the mean values. Dynamic height contours are adjusted as in Fig. 2. (b) Transport as a function of dynamic height contour in 0.1-dynamic-m bins, averaged zonally around the ACC. Dashed line is transport relative to the bottom determined from atlas data. Dots represent total transport including barotropic transport.

1–3 cm s^{-1} and imply a strong eastward transport in excess of what would be inferred from hydrography alone.

The results in Table 2 indicate that bottom velocities are eastward under eastward-flowing portions of the ACC and negative under westward-flowing segments of the Southern Ocean, regardless of mapping length scales. In general, bottom velocities have larger magnitudes when shorter meridional mapping decorrelation length scales are used, corresponding to lower smoothing. Case I, which assumes that streamfunction is strongly correlated along a priori contours of streamfunction, results in a strongly intensified jet flow, large apparent bottom flows, and an implied barotropic transport of 100×10^6 m^3 s^{-1}. Some of this difference may be attributed to the mismatch in decorrelation scales used for mapping hydrography as compared with those used to map float data. Bottom velocities are also sensitive to reference depth and to the signal-to-noise ratio, but the parameter ranges tested for this study do not result in significant variations in the results.

Overall, these results agree with those of Donohue et al. (2001) in predicting eastward bottom flow below the core of the ACC but (except for case I) suggest smaller bottom velocities than the ADCP data did. Bottom velocities in this study are sensitive to mapping scales. Altimetric observations imply that the most appropriate lengthscales are 100–200 km (Gille 1994), corresponding to mapping case F, which indicates an eastward bottom velocity of 3.3 ± 0.4 cm s^{-1}. This value is slightly smaller than the 4–10 cm s^{-1} range identified by Donohue et al. (2001). This difference in size may be an artifact of the smoothing used in the objective mapping, of the internal wave and tidal residuals in the ADCP fields, or of the east–west orientation of the ACC in the sections studied by Donohue et al. (2001).

On the basis of current meter data south of Australia, Phillips and Rintoul (2002) estimated that subantarctic front (SAF) transport estimates relative to the bottom captured 86% of the absolute transport. In comparison, using Pacific Ocean ADCP measurements, Donohue et al. (2001) suggested that SAF transport relative to the bottom could represent less than 50% of the absolute transport. The transport results derived here for the full Southern Ocean fall in between these two regional estimates, suggesting that the transport of the ACC core (which is dominated by the SAF) relative to the bottom represents about two-thirds of the total transport. These results also show that this eastward bottom flow is confined to a narrow jet and that the transport underestimate depends on the latitudinal span of the region considered as well as the spatial smoothing applied in the analysis.

5. Mean flow and bathymetric steering

As the mean dynamic topography maps in Fig. 2 indicate, bathymetry strongly influences the ACC, by steering the flow around ridges and through fracture zones, resulting in the ACC's zonally varying mean path. For example, evidence indicates that the SAF passes around Campbell Plateau (55°S, 170°E) and through the Eltanin Fracture Zone (55°S, 125°W) and the polar front passes through the Udintsev Fracture Zone (55°S, 140°W) in the Pacific–Antarctic Ridge (Gordon 1986; Gille 1994).

Potential vorticity (PV) constraints offer a means to evaluate bathymetric steering. If the ACC were fully barotropic, potential vorticity constraints would require flow to follow contours of f/H, where f is the Coriolis parameter and H is depth, and would roughly follow depth contours in regions where Coriolis parameter

changes were small. LaCasce (2000) has shown that floats are more likely to flow along contours of f/H than across them.

The ACC is not barotropic but has been characterized as being equivalent barotropic (Killworth 1992), implying that the flow is unidirectional from top to bottom and that velocities can be represented by a simple functional form that depends only on depth and surface velocity. A number of studies have taken advantage of the equivalent barotropic framework to derive potential vorticity conservation relations for equivalent barotropic flow (Gille 1995; Marshall 1995; Krupitsky et al. 1996). As an example, assume that velocity varies in the vertical direction following an exponential form,

$$\mathbf{u} = \mathbf{u}_s \exp\left(-\frac{z}{H_o}\right), \tag{1}$$

where $\mathbf{u}_s$ is the surface velocity, z is depth within the water column and is defined to be positive, and H_o is an e-folding depth. For the float data, which is at 900-m depth, $\mathbf{u}_s = \mathbf{u}(900)\exp(900/H_o)$. Then a PV conservation relationship can be written

$$J\left(\psi, \frac{f}{F_o}\right) = 0, \tag{2}$$

where $F_o = H_o[1 - \exp(-H/H_o)]$, and H is the ocean depth [see, e.g., Gille (1995) or Krupitsky et al. (1996)]. If flow is steered by bathymetry, then velocity vectors should be aligned along contours of f/F_o. In the limit where H_o is small, this is equivalent to having flow align along contours of f, while the limit of large H_o corresponds to f/H. There are clear limits to the utility of this example since vorticity is strongly forced in the Southern Ocean. Detailed analysis of the vorticity balance suggest that the appropriate e-folding depth is not sufficiently uniform to allow use of the equivalent barotropic PV equation as a diagnostic of variations in vorticity forcing (Gille 1997), although the large-scale balance should hold.

For this investigation, bathymetric data at 2′ resolution produced by Smith and Sandwell (1997) have been smoothed over length scales of 2°, 3°, or 4° longitude and an equivalent distance in latitude by applying a 60-, 90-, or 120-point Hanning filter twice in each direction. This eliminates high-wavenumber variability that may have little influence on large-scale ocean circulation while retaining the large-scale bathymetric features that are expected to control the flow.

To evaluate whether flow follows contours of f/F_o, the angular separation between $\mathbf{u}$ and the direction normal to $\nabla(f/F_o)$ was computed. If f/F_o were exactly conserved along streamlines, then the angular separation would consistently be zero, and its standard deviation would be low. In contrast, if angles were distributed evenly between $-\pi$ and π, the standard deviation would be 1.83. Figure 6 shows the standard deviation of angular separation as a function of H_o.

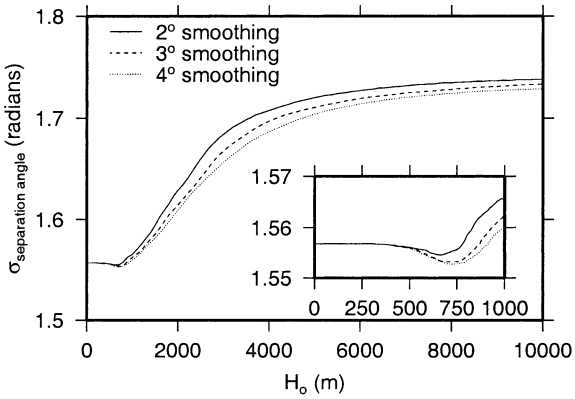

FIG. 6. Standard deviation of angular separation between float velocities and direction of mean f/F_o contours, as a function of e-folding scale H_o, where $F_o = H_o[1 - \exp(-H/H_o)]$. Solid, dashed, and dotted lines correspond to different degrees of filtering applied to bathymetry. The inset enlarges the standard deviations for low H_o to show the minimum around 700 m.

For values of H_o less than about 1000 m, the standard deviation is relative constant near 1.56. Mean angular separations are not statistically distinguishable from zero. Angular separations have low standard deviations for small values of H_o, in part because Southern Ocean winds are strongly zonal, and ocean circulation is therefore likely to follow contours of f regardless of vorticity constraints. For larger values of H_o, the standard deviation rises rapidly, indicating that unlike a barotropic flow, the Southern Ocean is not closely steered by contours of f/H. The smallest standard deviations of angular separation for all three levels of topographic smoothing occur when H_o = 657, 713, and 722 m for filtering on length scales of 2°, 3°, and 4°, respectively. This suggests that by a small margin, the Southern Ocean is best represented as having a topographically steered equivalent barotropic flow with an e-folding depth of about 700 m.

6. Summary

This study has focused on the mean dynamic height and temperature fields of the Circumpolar Current as inferred from ALACE float observations. The dense spatial sampling and absolute velocities measured by ALACE offer insights into Southern Ocean circulation that cannot be gleaned from hydrography alone. Results from ALACE floats indicate sharper temperature gradients and more narrowly concentrated circumpolar flow than are mapped in hydrographic atlas data. Temperature differences between ALACE and atlas data suggest that, when the ALACE data were collected during the 1990s, the Southern Ocean was warmer than its historic average.

Differences between geostrophic velocities derived from atlas and ALACE data imply eastward bottom velocities of 1–3 cm s^{-1} below the core of the ACC jets,

with westward bottom velocities outside the jet cores. Such a jet structure is consistent with numerical model predictions (e.g., Webb et al. 1991; Donohue et al. 2001) and ADCP analyses of the ACC (Donohue et al. 2001) showing significant eastward bottom velocities below eastward flowing currents in the Southern Ocean. This analysis suggests increases in net eastward transport of $10–30 \times 10^6$ m^3 s^{-1}, and the existence of nonzero bottom velocities implies that transports of deep and bottom water between ocean basins are larger than previous estimates might have assumed. Bottom velocities can influence the overall momentum balance of the system; for example, even in the simple framework in which bottom drag depends on the strength of the bottom velocities, stronger bottom velocities will correspond to stronger bottom drag.

Dynamic topography maps suggest that the flow in the ACC is steered by bathymetry. Detailed analysis of angular deviations between contours of potential vorticity and ALACE velocities indicates that the flow is steered by bathymetry, and that the most successful representation assumes that the flow is equivalent barotropic with an *e*-folding scale of 700 m. In addition to providing a way to estimate mean fields, ALACE also offers information on eddy statistics, as addressed in Part II of this study (Gille 2003).

Acknowledgments. Russ Davis contributed to this research, both by developing and deploying the ALACE floats and by commenting on the data analysis and interpretation. This research also would not have been possible without the efforts of numerous WOCE investigators who took the time to release ALACE floats over the course of research cruises to the remote parts of the Southern Hemisphere. Victor Gouretski of the WOCE analysis center in Hamburg helped both by making atlas data available and by answering detailed questions about the atlas product. In addition, the reviewers' comments have helped to clarify the presentation of this work. This research was supported by the National Science Foundation under Grant OCE-9985203/OCE-0049066 and by the National Aeronautics and Space Administration under JPL Contract 1224031.

APPENDIX

Anisotropic Objective Mapping of Streamfunctions

Objective mapping provides a formal methodology to map irregularly spaced measurements onto a regular grid (or any other desired coordinates), while minimizing error. The a priori covariance of the field is used to determine the weights assigned to each measurement and the formal error for the resulting mapped quantities. For oceanographic applications, Bretherton et al. (1976) outlined a method for producing objective maps of streamfunctions from velocity data as well as scalar quantities such as temperature. This method has also been widely applied in the atmosphere (e.g., Gandin 1965; Daley 1991). Maps of scalar quantities are relatively straightforward and easily adapted for special applications. This appendix reviews the method for mapping streamfunctions, and derives the general case using an anisotropic (but symmetric) covariance function. It also looks at a variation in which the covariance function has a dependence on an additional quantity, such as temperature or a priori dynamic height.

a. The general formulation: Mapping streamfunctions with a known covariance

To begin with, assume an a priori covariance function for the streamfunction, ψ, so that $\langle \psi(x, y)\psi(x + r, y + s)\rangle = F(\rho)$, where $\rho = \rho(r, s)$. If the field is nondivergent, then $u = -\partial\psi/\partial y$ and $v = \partial\psi/\partial x$. (The Coriolis term is included in u and v for this discussion.) From this, as discussed by Bretherton et al. (1976), the covariance functions relating ψ to u or v can be derived, as well as the velocity covariance functions:

$$\begin{aligned}\langle \psi(x, y)u(x + r, y + s)\rangle &= -\left\langle \psi(x, y)\frac{\partial}{\partial y}\psi(x + r, y + s)\right\rangle \\ &= -\frac{\partial}{\partial s}\langle \psi(x, y)\psi(x + r, y + s)\rangle = -\frac{\partial\rho}{\partial s}\frac{dF(\rho)}{d\rho}. \quad \text{(A1)}\end{aligned}$$

Correspondingly,

$$\langle \psi(x, y)v(x + r, y + s)\rangle = \frac{\partial\rho}{\partial r}\frac{dF(\rho)}{d\rho}. \quad \text{(A2)}$$

The velocity covariances are

$$\begin{aligned}\langle u(x, y)u(x + r, y + s)\rangle &= \left\langle \frac{\partial}{\partial y}\psi(x, y)\frac{\partial}{\partial y}\psi(x + r, y + s)\right\rangle \\ &= \frac{\partial}{\partial y}\left\langle \psi(x, y)\frac{\partial}{\partial y}\psi(x + r, y + s)\right\rangle \\ &\quad - \left\langle \psi(x, y)\frac{\partial^2}{\partial y^2}\psi(x + r, y + s)\right\rangle \\ &= \frac{\partial}{\partial y}\frac{\partial}{\partial s}\langle \psi(x, y)\psi(x + r, y + s)\rangle \\ &\quad - \frac{\partial^2}{\partial s^2}\langle \psi(x, y)\psi(x + r, y + s)\rangle \\ &= \frac{\partial}{\partial y}\left[\frac{\partial\rho}{\partial s}\frac{dF(\rho)}{d\rho}\right] - \frac{\partial}{\partial s}\left[\frac{\partial\rho}{\partial s}\frac{dF(\rho)}{d\rho}\right] \\ &= \frac{\partial}{\partial y}\left[\frac{\partial\rho}{\partial s}\frac{dF(\rho)}{d\rho}\right] - \frac{\partial^2\rho}{\partial s^2}\frac{dF(\rho)}{d\rho} - \left(\frac{\partial\rho}{\partial s}\right)^2\frac{d^2F(\rho)}{d\rho^2}, \quad \text{(A3)}\end{aligned}$$

$$\langle v(x, y)v(x + r, y + s)\rangle = \frac{\partial}{\partial x}\left[\frac{\partial \rho}{\partial r}\frac{dF(\rho)}{d\rho}\right] - \frac{\partial^2 \rho}{\partial r^2}\frac{dF(\rho)}{d\rho} - \left(\frac{\partial \rho}{\partial r}\right)^2 \frac{d^2F(\rho)}{d\rho^2}, \quad \text{(A4)}$$

$$\langle u(x, y)v(x + r, y + s)\rangle = \langle v(x + r, y + s)u(x, y)\rangle = -\frac{\partial}{\partial y}\left[\frac{\partial \rho}{\partial r}\frac{dF(\rho)}{d\rho}\right] + \frac{\partial^2 \rho}{\partial s \partial r}\frac{dF(\rho)}{d\rho} + \frac{\partial \rho}{\partial r}\frac{\partial \rho}{\partial s}\frac{d^2F(\rho)}{d\rho^2}. \quad \text{(A5)}$$

[Daley (1991), among others, provides an alternate derivation for the basic structure of these covariance equations.]

To estimate the streamfunction, first we define a column vector of velocity measurements $\boldsymbol{\phi}$, containing all u measurements and then all v measurements:

$$\boldsymbol{\phi} = [u_1\, u_2 \cdots u_N\, v_1\, v_2 \cdots v_N]^{\mathrm{T}}, \quad \text{(A6)}$$

where N is the number of vector velocity observations. The matrix $\mathbf{A}$ contains the covariances of $\boldsymbol{\phi}$ from (A3), (A4), and (A5):

$$\mathbf{A} = \langle \boldsymbol{\phi}\boldsymbol{\phi}^{\mathrm{T}}\rangle \quad \text{(A7)}$$

and is dimensioned $2N$ by $2N$. The matrix $\mathbf{P}$ holds the covariances of $\boldsymbol{\psi}$ with $\boldsymbol{\phi}$ from (A1) and (A2):

$$\mathbf{P} = \langle \boldsymbol{\phi}\boldsymbol{\psi}\rangle \quad \text{(A8)}$$

and is dimensioned $2N$ by N. The vector $\boldsymbol{\psi}$ contains N values corresponding to streamfunction at each of the locations where velocity was measured.

Data are noisy as compared with true values of velocity or streamfunction because of measurement errors and because data measure mesoscale and time-varying structures that will appear like noise in the mean fields. The scalar ϵ represents the variance due to the differences between instantaneous and smoothed fields; ϵ is added to the diagonal of $\mathbf{A}$ to represent the effective increase in autocovariance due to measurement noise. Adding noise along the diagonal has the added benefit of making $\mathbf{A} + \epsilon\mathbf{I}$ diagonally dominant and therefore easier to invert. Using the covariance matrices $\mathbf{P}$ and $\mathbf{A}$, we seek an estimate $\hat{\boldsymbol{\psi}}$ of the true streamfunction $\boldsymbol{\psi}$:

$$\hat{\boldsymbol{\psi}} = \mathbf{P}(\mathbf{A} + \epsilon\mathbf{I})^{-1}\boldsymbol{\phi}. \quad \text{(A9)}$$

The squared error in $\boldsymbol{\psi}$ is

$$\frac{(\hat{\boldsymbol{\psi}} - \boldsymbol{\psi})^2}{\boldsymbol{\psi}^2} = 1 - \frac{\mathbf{P}(\mathbf{A} + \epsilon\mathbf{I})^{-1}\mathbf{P}}{\mathrm{diag}(\mathbf{P})}. \quad \text{(A10)}$$

b. The basic case: Isotropic and anisotropic decorrelation

Bretherton et al. (1976) assumed that the covariance of $\langle \psi\psi\rangle$, $F(\rho)$, was isotropic in space so that $\rho^2 = r^2 + s^2$. For example, F could define an isotropic Gaussian decorrelation that depends only on the distance between observations. In the Southern Ocean, tracers can be advected zonally with the mean current. Previous analyses have suggested that temperature and dynamic height decorrelate more quickly in the meridional direction than in the zonal direction (Olbers et al. 1992; Gille 1994). Here the covariance functions are adapted to account for an anisotropic but symmetric decorrelation scale.

Assume $F = F(r/L_x, s/L_y) = F(\rho)$, where $\rho^2 = (r/L_x)^2 + (s/L_y)^2$, then

$$\frac{\partial \rho}{\partial r} = \frac{r}{\rho L_x^2}, \quad \text{(A11)}$$

$$\frac{\partial \rho}{\partial s} = \frac{s}{\rho L_y^2}, \quad \text{(A12)}$$

$$\frac{\partial^2 \rho}{\partial r^2} = \frac{1}{\rho L_x^2}\left(1 - \frac{r^2}{\rho^2 L_x^2}\right), \quad \text{(A13)}$$

and so forth. Since ρ has no dependence on geographic position, all x and y derivatives are zero. Substituting these relations into (A1)–(A5) yields the following covariances:

$$\langle \psi(x, y)u(x + r, y + s)\rangle = -\frac{s}{L_y^2 \rho_o}\frac{dF}{d\rho_o}, \quad \text{(A14)}$$

$$\langle \psi(x, y)v(x + r, y + s)\rangle = \frac{r}{L_x^2 \rho_o}\frac{dF}{d\rho_o}, \quad \text{(A15)}$$

$$\langle u(x, y)u(x + r, y + s)\rangle = \frac{1}{L_y^2}\left[-\left(1 - \frac{s^2}{L_y^2 \rho_o^2}\right)\frac{1}{\rho_o}\frac{dF}{d\rho_o} - \frac{s^2}{\rho_o^2 L_y^2}\frac{d^2F}{d\rho_o^2}\right], \quad \text{(A16)}$$

$$\langle v(x, y)v(x + r, y + s)\rangle = \frac{1}{L_x^2}\left[-\left(1 - \frac{r^2}{\rho_o^2 L_x^2}\right)\frac{1}{\rho_o}\frac{dF}{d\rho_o} - \frac{r^2}{\rho_o^2 L_x^2}\frac{d^2F}{d\rho_o^2}\right], \quad \text{(A17)}$$

$$\langle u(x, y)v(x + r, y + s)\rangle = \langle v(x, y)u(x + r, y + s)\rangle = \frac{rs}{\rho_o^2 L_x^2 L_y^2}\left(-\frac{1}{\rho_o}\frac{dF}{d\rho_o} + \frac{d^2F}{d\rho_o^2}\right). \quad \text{(A18)}$$

In the limit where $L_x = L_y = 1$, Eqs. (A14)–(A18) reduce to the isotropic form derived by Bretherton et al. (1976). In the results presented here, cases A, B, G, H, J, and K use isotropic covariance functions, while cases C–F use anisotropic covariances. In all cases, a Gaussian decorrelation function is assumed. In contrast with the analytic covariance functions presented here, velocity covariances could also be determined by computing discrete derivatives of $\langle \psi\psi\rangle$ (e.g., Davis 1998).

Since the covariance functions are really estimates of the covariance between velocity and streamfunction anomalies, mean velocities should be removed from ϕ

before mapping and a mean streamfunction added to ψ at the end. For this purpose, dynamic topography estimated from gridded atlas data was used (Gouretski and Jancke 1998).

While ρ is easily calculated in the isotropic case as the angular separations between two points on a sphere, in the anisotropic case, the zonal and meridional separations, r and s, must be determined individually. For this study, s was computed from the latitudinal separation, ρ was determined as the total distance between two points, and then the length of r was defined as $|r| = \sqrt{\rho^2 - s^2}$, with the sign of r adjusted appropriately.

c. Variation: Covariances that depend on other quantities

The methodology discussed above is easily adapted to handle more complicated covariance functions. If streamlines follow contours of temperature, depth, or f/H, then the covariance functions can be modified to take this into account. As an illustration, here we define a function G that varies with position. Suppose that the streamfunction is relatively constant along contours of G but changes rapidly across regions where G changes. Then we can define a scalar $\rho_G^2 = (r/L_x)^2 + (s/L_y)^2 + (g/L_G)^2$, where $g = G(x + r, y + s) - G(x, y) = G_2 - G_1$, such that $\langle \psi(x, y)\psi(x + r, y + s)\rangle = F(\rho_g)$. Based on the definition of ρ_G,

$$\frac{\partial \rho_G}{\partial s} = \frac{s}{\rho_G L_y^2} + \frac{g}{\rho_G L_G^2}\frac{\partial G_2}{\partial y}, \tag{A19}$$

$$\frac{\partial \rho_G}{\partial y} = +\frac{g}{\rho_G L_G^2}\frac{\partial (G_2 - G_1)}{\partial y}. \tag{A20}$$

By substituting (A19) and (A20) and the related x and r derivatives into (A1)–(A5), we can derive all of the covariance functions required to map the data.

From this the covariances are

$$\langle \psi(x, y)u(x + r, y + s)\rangle = -\left(\frac{s}{\rho_G L_y^2} + \frac{gG_{2y}}{L_G^2 \rho_G}\right)\frac{dF}{d\rho_G}, \tag{A21}$$

$$\langle \psi(x, y)v(x + r, y + s)\rangle = \left(\frac{r}{\rho_G L_x^2} + \frac{gG_{2x}}{L_G^2 \rho_G}\right)\frac{dF}{d\rho_G}, \tag{A22}$$

$$\langle u(x, y)u(x + r, y + s)\rangle = \frac{1}{\rho_G}\left[-\frac{1}{L_y^2} - \frac{G_{1y}G_{2y}}{L_G^2} + \frac{1}{\rho_G^2}\left(\frac{s}{L_y^2} + \frac{gG_{1y}}{L_G^2}\right)\left(\frac{s}{L_y^2} + \frac{gG_{2y}}{L_G^2}\right)\right]\frac{dF}{d\rho_G} - \frac{1}{\rho_G^2}\left(\frac{s}{L_y^2} + \frac{gG_{1y}}{L_G^2}\right)\left(\frac{s}{L_y^2} + \frac{gG_{2y}}{L_G^2}\right)\frac{d^2F}{d\rho_G^2}, \tag{A23}$$

$$\langle v(x, y)v(x + r, y + s)\rangle = \frac{1}{\rho_G}\left[-\frac{1}{L_x^2} - \frac{G_{1x}G_{2x}}{L_G^2} + \frac{1}{\rho_G^2}\left(\frac{r}{L_x^2} + \frac{gG_{1x}}{L_G^2}\right)\left(\frac{r}{L_x^2} + \frac{gG_{2x}}{L_G^2}\right)\right]\frac{dF}{d\rho_G} - \frac{1}{\rho_G^2}\left(\frac{r}{L_x^2} + \frac{gG_{1x}}{L_G^2}\right)\left(\frac{r}{L_x^2} + \frac{gG_{2x}}{L_G^2}\right)\frac{d^2F}{d\rho_G^2}, \tag{A24}$$

$$\langle u(x, y)v(x + r, y + s)\rangle = \frac{1}{\rho_G}\left[+\frac{G_{2x}G_{1y}}{L_G^2} - \frac{1}{\rho_G^2}\left(\frac{r}{L_x^2} + \frac{gG_{2x}}{L_G^2}\right)\left(\frac{s}{L_y^2} + \frac{gG_{1y}}{L_G^2}\right)\right]\frac{dF}{d\rho_G} + \frac{1}{\rho_G^2}\left(\frac{r}{L_x^2} + \frac{gG_{2x}}{L_G^2}\right)\left(\frac{s}{L_y^2} + \frac{gG_{1y}}{L_G^2}\right)\frac{d^2F}{d\rho_G^2}, \tag{A25}$$

where partial derivatives of G are indicated by subscripts (e.g., $G_{1x} = \partial G_1/\partial x$). In practical implementations, if G is an observed quantity, such as f/H, then (A21)–(A25) are calculated by computing discrete derivatives. As with zonal and meridional decorrelation scales, large values of L_G have little impact on the covariances, while small values force the streamlines to align with contours of G. This scenario is tested in objective mapping case I, discussed in section 4.

Last, with a little algebra, the covariances defined by (A1)–(A5) can be modified in the special case in which the amplitude of the covariance varies spatially, so $\langle \psi(x, y)\psi(x + r, y + s)\rangle = A(x, y)A(x + r, y + s)F(\rho)$. This structure was not implemented for the current study and is not discussed here.

REFERENCES

Antonov, J., S. Levitus, T. P. Boyer, M. E. Conkright, T. D. O'Brien, and C. Stephens, 1998: *Temperature of the Atlantic Ocean.* Vol. 1, *World Ocean Atlas 1998*, NOAA Atlas NESDIS 27, 167 pp.

Bretherton, F. P., R. E. Davis, and C. B. Fandry, 1976: A technique for objective analysis and design of oceanographic experiments applied to MODE-73. *Deep-Sea Res.*, **23,** 559–582.

Daley, R., 1991: *Atmospheric Data Analysis*. Cambridge University Press, 471 pp.

Davis, R. E., 1998: Preliminary results from directly measuring mid-

depth circulation in the tropical and South Pacific. *J. Geophys. Res.*, **103,** 24 619–24 639.
——, P. D. Killworth, and J. R. Blundell, 1996: Comparison of autonomous Lagrangian circulation explorer and fine resolution Antarctic model results in the South Atlantic. *J. Geophys. Res.*, **101,** 855–884.
——, J. T. Sherman, and J. Dufour, 2001: Profiling ALACEs and other advances in autonomous subsurface floats. *J. Atmos. Oceanic Technol.*, **18,** 982–993.
Donohue, K. A., E. Firing, and S. Chen, 2001: Absolute geostrophic velocity within the Subantarctic Front in the Pacific Ocean. *J. Geophys. Res.*, **106,** 19 869–19 882.
Gandin, L. S., 1965: *Objective Analysis of Meteorological Fields.* Israel Program for Scientific Translations, 242 pp.
Georgi, D. T., and J. M. Toole, 1982: The Antarctic Circumpolar Current and the oceanic heat and freshwater budgets. *J. Mar. Res.*, **40S,** 183–197.
Gille, S. T., 1994: Mean sea surface height of the Antarctic Circumpolar Current from Geosat data: Method and application. *J. Geophys. Res.*, **99,** 18 255–18 273.
——, 1995: Dynamics of the Antarctic Circumpolar Current: Evidence for topographic effects from altimeter data and numerical model output. Ph.D. thesis, MIT/Woods Hole Oceanographic Institution Joint Program, 216 pp.
——, 1997: Why potential vorticity is not conserved along mean streamlines in a numerical Southern Ocean. *J. Phys. Oceanogr.*, **27,** 1286–1299.
——, 1999: Mass, heat, and salt transport in the southeastern Pacific: A circumpolar current inverse model. *J. Geophys. Res.*, **104,** 5191–5210.
——, 2002: Warming of the Southern Ocean since the 1950s. *Science*, **295,** 1275–1277.
——, 2003: Float observations of the Southern Ocean. Part II: Eddy fluxes. *J. Phys. Oceanogr.*, **33,** 1182–1196.
Gordon, A. L., 1986: Interocean exchange of thermocline water. *J. Geophys. Res.*, **91,** 5037–5046.
——, E. Molinelli, and T. Baker, 1978: Large-scale relative dynamic topography of the Southern Ocean. *J. Geophys. Res.*, **83,** 3023–3032.
Gouretski, V. V., and K. Jancke, 1998: A new climatology for the World Ocean. WHP SAC Tech. Rep. 3, WOCE Rep. 162/98, WOCE Special Analysis Centre, Max Planck Institute, Hamburg, Germany.
Hogg, N. G., 1991: Mooring motion corrections revisited. *J. Atmos. Oceanic Technol.*, **8,** 289–295.
Kamenkovich, V. M., 1962: On the theory of the Antarctic Circumpolar Current (in Russian with English abstract). *Tr. Inst. Okeanol.*, **56,** 241–293.
Killworth, P. D., 1992: An equivalent-barotropic mode in the Fine Resolution Antarctic Model. *J. Phys. Oceanogr.*, **22,** 1379–1387.
Krupitsky, A., V. Kamenkovich, N. Naik, and M. A. Cane, 1996: A linear equivalent barotropic model of the Antarctic Circumpolar Current with realistic coastlines and bottom topography. *J. Phys. Oceanogr.*, **26,** 1803–1824.
LaCasce, J. H., 2000: Floats and f/H. *J. Mar. Res.*, **58,** 61–95.
Levitus, S., and T. P. Boyer, 1994: *Temperature*. Vol. 4, *World Ocean Atlas 1994*, NOAA Atlas NESDIS 4, 117 pp.
——, and Coauthors, 1998: *Introduction.* Vol. 1, *World Ocean Database 1998*, NOAA Atlas NESDIS 18, 346 pp.
Marshall, D., 1995: Influence of topography on the large-scale ocean circulation. *J. Phys. Oceanogr.*, **25,** 1622–1635.
Nowlin, W. D., Jr., and J. M. Klinck, 1986: The physics of the Antarctic Circumpolar Current. *Rev. Geophys.*, **24,** 469–491.
Olbers, D., V. Gouretski, G. Seiß, and J. Schröter, 1992: *Hydrographic Atlas of the Southern Ocean.* Alfred Wegener Institute, 17 pp. and 82 plates.
Phillips, H. E., and S. R. Rintoul, 2002: A mean synoptic view of the Subantarctic Front south of Australia. *J. Phys. Oceanogr.*, **32,** 1536–1553.
Saunders, P. M., and N. P. Fofonoff, 1976: Conversion of pressure to depth in the ocean. *Deep-Sea Res.*, **23,** 109–111.
Schulman, E. E., 1975: A study of topographic effects. *Numerical Models of Ocean Circulation*, Ocean Studies Board, National Academy of Science, 147–165.
Smith, W. H. F., and D. T. Sandwell, 1997: Global seafloor topography from satellite altimetery and ship depth soundings. *Science*, **277,** 1956–1962.
Swift, J. H., 1995: Comparing WOCE and historical temperatures in the deep southeast Pacific. Int. WOCE Newsletter, No. 18, WOCE International Project Office, Southampton, United Kingdom, 15–17.
Webb, D. J., P. D. Killworth, A. C. Coward, and S. R. Thompson, 1991: *The FRAM Atlas of the Southern Ocean.* Natural Environment Research Council, 67 pp.
Whitworth, T. I., and W. D. Nowlin Jr., 1987: Water masses and currents of the Southern Ocean at Greenwich meridian. *J. Geophys. Res.*, **92,** 6462–6476.
——, ——, and S. J. Worley, 1982: The net transport of the Antarctic Circumpolar Current through Drake Passage. *J. Phys. Oceanogr.*, **12,** 960–971.
Wunsch, C., 1996: *The Ocean Circulation Inverse Problem.* Cambridge University Press, 442 pp.